APL Materials

# Deconvoluting the energy transport mechanisms in all-inorganic $CsPb_2Br_5$/$CsPbBr_3$ perovskite composite systems

Cite as: APL Mater. **10**, 031101 (2022); https://doi.org/10.1063/5.0083022
Submitted: 21 December 2021 • Accepted: 07 February 2022 • Published Online: 03 March 2022

Yunpeng Wang, Fei Wang, Gangbei Zhu, et al.

# Deconvoluting the energy transport mechanisms in all-inorganic $CsPb_2Br_5/CsPbBr_3$ perovskite composite systems

Cite as: APL Mater. 10, 031101 (2022); doi: 10.1063/5.0083022
Submitted: 21 December 2021 • Accepted: 7 February 2022 •
Published Online: 3 March 2022



Yunpeng Wang,[1] Fei Wang,[1,2,3,a)] Gangbei Zhu,[4] Quan Quan,[2] Zhengxun Lai,[2] You Meng,[2] Yi Fan,[1] SenPo Yip,[5] Dongxu Zhao,[1,a)] and Johnny C. Ho[2,3,5,a)]

## AFFILIATIONS

[1] State Key Laboratory of Luminescence and Applications, Changchun Institute of Optics, Fine Mechanics and Physics, Chinese Academy of Sciences, Changchun 130033, China
[2] Department of Materials Science and Engineering, City University of Hong Kong, Kowloon, Hong Kong SAR 999077, China
[3] State Key Laboratory of Terahertz and Millimeter Waves, City University of Hong Kong, Kowloon, Hong Kong SAR 999077, China
[4] National Key Laboratory of Shock Wave and Detonation Physics, Institute of Fluid Physics, China Academy of Engineering Physics, Mianyang 621900, China
[5] Institute for Materials Chemistry and Engineering, Kyushu University, Fukuoka 816-8580, Japan

[a)] **Authors to whom correspondence should be addressed:** wangf@ciomp.ac.cn; zhaodx@ciomp.ac.cn; and johnnyho@cityu.edu.hk

## ABSTRACT

$CsPb_2Br_5/CsPbBr_3$ composite systems have received considerable attention among numerous lead halide perovskite materials due to their significantly enhanced photoluminescence intensity and stability against moisture. However, the luminescence mechanism of $CsPb_2Br_5$ based materials remains controversial, which significantly hinders the further material design and utilization for optoelectronic devices. In this work, to deconvolute their luminescent mechanisms, high-quality $CsPb_2Br_5$ crystals without any undesired by-products and impurities have been first prepared by a microwave-assisted synthesis method. The luminescence-inactive characteristics of the material are then confirmed by the steady-state absorption, photoluminescence, transient absorption spectra, and time-resolved terahertz spectroscopy. The prepared $CsPb_2Br_5$ crystals exhibit excellent crystallinity and enhanced thermal stability, particularly that they can maintain their crystalline structures in polar organic solvents. By simply manipulating the ratios of different precursor materials, it is witnessed that the green emission comes from the $CsPbBr_3$ adhered, nucleated, and grown on the $CsPb_2Br_5$ crystals. Ultrafast transient absorption measurements in visible and terahertz spectral regions reveal that with the help of phonon scattering-assisted hopping at interfacial states, intersystem crossing dominates the electron transfer process in the composite crystals. As a result, the $CsPb_2Br_5$ and $CsPbBr_3$ interact extensively with each other. Meanwhile, the Auger recombination rate and the defect-related non-radiative process are suppressed in the composite crystals, thereby enhancing the fluorescence of composite crystals. This work has not only deconvoluted the controversial and unclear luminescent mechanisms of $CsPb_2Br_5$ materials but also established a pathway to design and enhance the fluorescence of materials for technological applications.



## INTRODUCTION

Cesium lead bromide (Cs–Pb–Br) perovskites are excellent candidate materials for next-generation lighting and display devices due to their superb properties of highly efficient and stable luminescence, narrow fluorescent line widths, and easily tunable emission wavelengths.[1–3] Typically, there are three main structures explored and reported for Cs–Pb–Br perovskites: $CsPbBr_3$, $CsPb_2Br_5$, and $Cs_4PbBr_6$, which can be obtained by changing the stoichiometry ratio between CsBr and $PbBr_2$ precursors during the

synthetic process.[4] Until now, extensive research efforts have been dedicated to examining and deciphering the structural, optical, and electronic properties of these three perovskite materials.[5–11] It is worth mentioning that the synthesized $CsPb_2Br_5/CsPbBr_3$ composite structures have not only shown the increased photoluminescence (PL) intensity arising from the dielectric confinement of $CsPb_2Br_5$ material but also present the much-enhanced stability against moisture owing to the water-resistant characteristics of the $CsPb_2Br_5$ matrix.[8] These $CsPb_2Br_5/CsPbBr_3$ perovskite complexes can then almost keep their initial PL intensity after four months of storage in an ambient atmosphere.[5] They can even retain their high PL quantum yields and narrow-band emissions in water solutions.[6] In this regard, the $CsPb_2Br_5$ and $CsPb_2Br_5/CsPbBr_3$ composite materials have become a hot research topic for their potential possibilities to resolve the instability issues of perovskites, drawing substantial attention in recent years.[9]

It is encouraging that the PeLED (perovskite light-emitting diode) fabricated from $CsPb_2Br_5/CsPbBr_3$ nanocrystals exhibited better operational stability, higher external quantum efficiency (EQE), and longer operational lifetime in comparison with single-phase $CsPbBr_3$ materials.[7] Besides moisture and water, the $CsPb_2Br_5/CsPbBr_3$ core/shell nanocrystals also possess significantly increased stability and PL quantum yields against heat and ultraviolet light irradiation.[8] Recent reports on $CsPbBr_3/CsPb_2Br_5$ @PbBr(OH) nano-/microspheres have shown an outstanding PL quantum yield of ~98%. They can surprisingly maintain their excellent PL intensity and high quantum yield when immersed in water for even more than 18 months.[9] Furthermore, the low-threshold amplified spontaneous emission (ASE) can be generated from the $CsPb_2Br_5$ microplates under one- and two-photon excitation.[10] The outstanding long-term stability can also be realized with the $CsPb_2Br_5/CsPbBr_3$ based solar cells.[11] All these results show the great application potentials of $CsPb_2Br_5$ based single-phase and complex perovskites for highly stable and high-performance photoelectric devices.

However, although there are many achievements and progress made on $CsPb_2Br_5$ and its related composite materials, it is still not clear about the exact luminescence mechanism of $CsPb_2Br_5$ based materials. For instance, it was calculated and reported that $CsPb_2Br_5$ has a broad indirect bandgap, indicating that it is PL inactive,[12,13] but the green fluorescence in $CsPb_2Br_5$ has also been widely observed.[10,14–18] There exists a severe inconsistency that emerged between the theoretical simulation and experimental results. The luminescence center of $CsPb_2Br_5$ is believed to arise from the secondary phase generated during the synthesis procedure, such as amorphous lead bromide ammonium complexes or $CsPbBr_3$ nanocrystals.[17,18] Also, the spatially distinguished electronic states in $CsPb_2Br_5$ were reported to be responsible for the green fluorescence.[10] A recent study based on first-principles calculations further suggests that vacancy ($V_{Br}$) and antisite defects (CsPb) may be the origin of green emissions in $CsPb_2Br_5$.[16] In any case, the current understanding of the mechanism is not sufficient. Even though $CsPb_2Br_5$ materials with green fluorescence have been claimed to be pure phases in some works, it is hard to exclude $CsPbBr_3$ nanocrystals or other luminescent centers when their concentrations are low. As a result, the actual bandgap and whether the green emission comes from embedded $CsPbBr_3$ nanocrystals or point defects, such as Br vacancies in $CsPb_2Br_5$, are not certain. Without solid experimental evidence, the luminescence mechanism of $CsPb_2Br_5$ based materials remains controversial in the community. This mechanism understanding is the enabling key factor for the practical utilization of $CsPb_2Br_5$ based devices.

Notably, those mentioned above contradicting experimental findings on the origins of luminescence in $CsPb_2Br_5$ seemed to deduce from the perovskite materials fabricated by different synthesis methods, heating sources, and process conditions.[17] In fact, the stoichiometric $CsPb_2Br_5$ is only stable within a very narrow and long area of chemical potentials to prevent forming all the possible competitive phases,[13,16] inferring that slight changes in the growth conditions would induce phase transformations and make the resultant $CsPb_2Br_5$ impure. That may explain why the experimental results of the optical properties of $CsPb_2Br_5$ are not consistent. Among these experimental results, there is some evidence but not certain about the correlation between intrinsic defects and green emissions in $CsPb_2Br_5$.[19] Therefore, it is extremely important to develop equilibrium thermodynamic systems to controllably synthesize pure and high-quality $CsPb_2Br_5$ crystals to examine their fundamental properties.

In this work, we employed a microwave-assisted synthesis method to grow pure $CsPb_2Br_5$ crystals. It is advantageous that microwave irradiation produces efficient internal heating and is capable of increasing the control volume temperature simultaneously and uniformly. This way, the microwave energy can be introduced into the chemical reactor remotely, building a direct access from the energy source to the reaction vessel. Once the microwave radiation passes through the vessel walls, it only heats up the reactants and solvents rather than the vessel itself. As a result, the temperature increase is uniform throughout the entire sample, leading to fewer decompose products as well as unwanted by-products.[20,21] More importantly, the reduced side reactions with the microwave-assisted synthesis are anticipated and later confirmed to enable the growth of high-quality $CsPb_2Br_5$ crystals in order to precisely explore its fundamental properties, helping to clarify the controversies on the bandgap of $CsPb_2Br_5$. Technically, as a PL-active material, the initial focus is to evaluate the physical nature of the emission process and the involved excited states $CsPb_2Br_5$; nevertheless, it is challenging to exclusively reveal the luminescence mechanism of the Cs–Pb–Br perovskite composite system by most simple spectral characterization.[17] Despite many clues that have been obscured in the ensemble-averaged measurements, fortunately, the ultrafast transient spectroscopy is capable of revealing the dynamics of charge carriers of the materials.[22] In such a way, experimental studies of ultrafast transient absorption (TA) and terahertz (THz) absorption spectroscopy are performed on the microwave-synthesized pure $CsPb_2Br_5$ crystals and their $CsPb_2Br_5/CsPbBr_3$ composite systems, where the findings directly lead to a more comprehensive and in-depth understanding of the associated PL mechanism of Cs–Pb–Br perovskites. These valuable insights of the fundamental PL mechanism of these perovskite materials would provide essential guidelines for further optimizing their PL properties for various technological applications.

## RESULTS AND DISCUSSION

Figure 1 shows the optical image of a $CsPb_2Br_5$ crystal, which presents a perfect quadrate morphology with smooth and clean

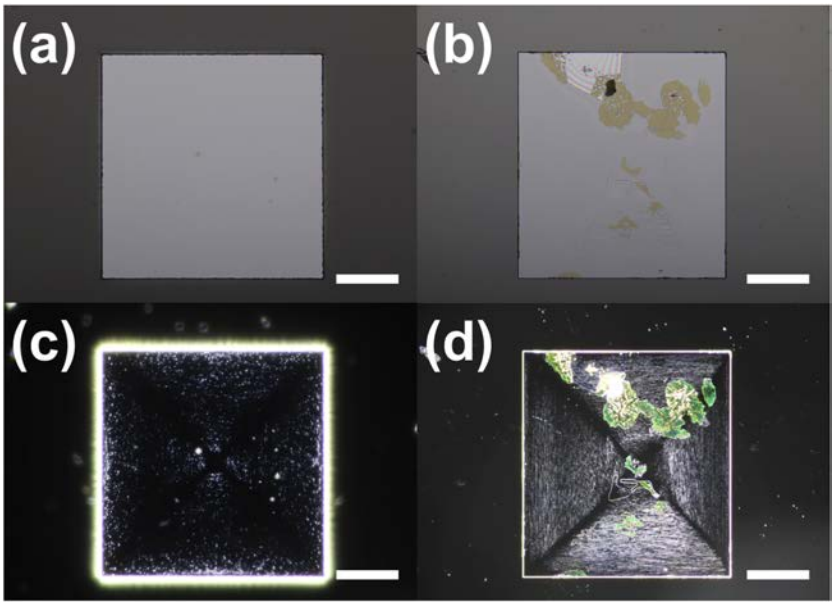


**FIG. 1.** Bright-field (a) and dark-field (c) microscopy images of a $CsPb_2Br_5$ crystal. Bright-field (b) and dark-field (d) microscopy images of a $CsPb_2Br_5$ crystal synthesized with the precursors ratio ($CsBr:PbBr_2$) of 0.6:1. Scale bars are 100 $\mu$m.

surfaces. The average size of the crystals is ~500 $\mu$m. Under the illumination of 360 nm light, the single crystal presents no luminescence in Fig. 1(c), which corresponds to the calculation results that $CsPb_2Br_5$ has an indirect bandgap. The luminescence from the $CsPb_2Br_5$ crystals is inactive, indicating no fluorescent $CsPbBr_3$ nano- or micro-crystals formed in the $CsPb_2Br_5$ crystals. The microwave-assisted synthesis method introduced here is again confirmed to effectively avoid the formation of any unwanted products due to the non-uniform temperature during material growth. Figures S1–S6 show the structural and steady-state optical properties of the crystals, while the high crystallinity, enhanced thermal stability, and luminescence-inactive characteristics of $CsPb_2Br_5$ crystals are evidently confirmed. However, when the precursor molar ratio is slightly increased from 0.5:1 ($CsBr:PbBr_2$) to 0.6:1, some yellow patches begin to appear on the surface of the $CsPb_2Br_5$ crystal [Fig. 1(b)]. Under the irradiation of 360 nm light, the patches or the spots start to emit the green light [Fig. 1(d)], which suggests that the $CsPbBr_3$ crystals have started to form on the $CsPb_2Br_5$ crystals.

In order to reveal the origin of the green fluorescence and to obtain further insights into the luminescent mechanisms of $CsPb_2Br_5/CsPbBr_3$ composite crystals, an ultrafast TA spectroscopy is taken to investigate the interaction between $CsPb_2Br_5$ and $CsPbBr_3$ in the composite crystals. Considering the steady-state absorption spectra of the crystals [Fig. S5(e)], a 400 nm pumping wavelength is chosen to stimulate $CsPbBr_3$ rather than $CsPb_2Br_5$. This way, the energy transfer process can be identified more clearly without any distraction. It is known that the excitation power density can affect the carrier dynamics as well as the transient absorption curves of the material.[23,24] Therefore, a low pump fluence of $\langle N \rangle = 0.1$ (3.85 $\mu J\ cm^{-2}$ at 400 nm) is utilized to record the TA spectrum for accordance with the fluorescent irradiation conditions, where $\langle N \rangle$ represents the average number of photons absorbed per nanocrystal per pulse obtained from the following equation:

$$I_{PL} = 1 - e^{-N} = 1 - e^{-\delta j_p}, \tag{1}$$

where $I_{PL}$ is the time-resolved PL intensity, $\delta$ is the absorption cross-section of the material, and $j_p$ is the per-pulse photon fluence.[25] As shown in Fig. 2(a), because the pumping wavelength is out of their absorption band, there are no signals observed in the ultrafast TA spectra of $CsPb_2Br_5$ crystals, which verifies again that pure $CsPb_2Br_5$ crystals have been prepared. Also, the corresponding time-dependent transient spectrograms with the delay time of 5, 10, 20, 40, and 100 ps are depicted in Fig. S7. However, different from Figs. 2(a) and S7(a), the TA signals of $CsPb_2Br_5/CsPbBr_3$ composite crystals become visible in Figs. 2(b) and 2(c). In addition, the TA spectra are as well taken for the $CsPbBr_3$ reference sample and shown in Figs. 2(d) and S7(d), which present bleaching peaks of the absorption band edge at ~530 nm due to the band filling, together with the excited-state absorption peaks centered at 500–520 nm. This strong absorption bleaching band at ~530 nm indicates that near band-edge transitions strongly dominate in $CsPbBr_3$, while the peak position and amplitude remain unchanged from 5 to 100 ps. Compared with the TA signals of $CsPb_2Br_5/CsPbBr_3$ composite crystals, there are several notable differences:

(i) The bleaching peaks of composite crystals have blue-shifted from 530 to ~520 nm.
(ii) The bleaching peaks of composite crystals are partially decayed.
(iii) The full width at half maximum (FWHM) of composite crystals' bleach peaks have narrowed down.
(iv) The excited state absorption peaks of composite crystals are reduced.
(v) There is also a distinct absorption signal that appeared at ~540 nm during the time region from 5 to 100 ps with the reducing amplitude.

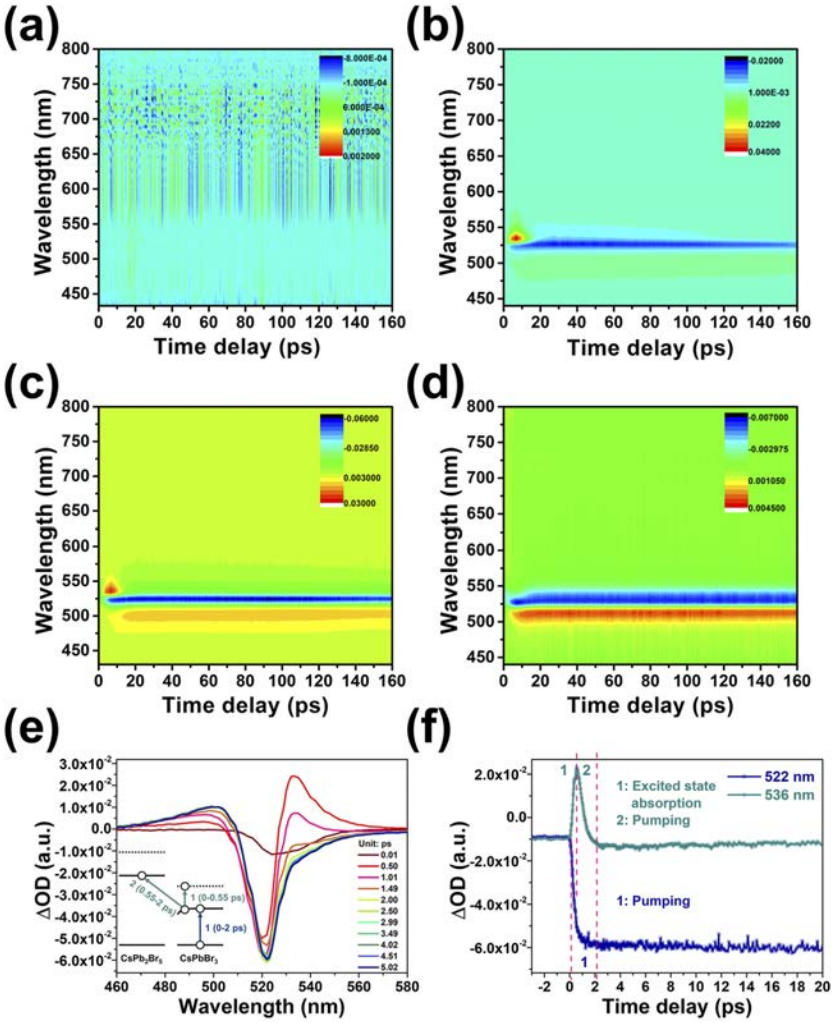


**FIG. 2.** Transient absorption evolution for $CsPb_2Br_5$ crystals (a), crystals synthesized with the precursor ratio ($CsBr:PbBr_2$) of 0.6:1 (b), 0.8:1 (c), and $CsPbBr_3$ crystals (d). (e) Time-resolved TA spectra of composite crystals synthesized with the precursor ratio ($CsBr:PbBr_2$) of 0.8:1. Inset is the diagram of electron transition. (f) TA signal kinetics at different wavelengths, indicating the electron transition from $CsPbBr_3$ to $CsPb_2Br_5$.

The observed blue-shift of ground-state bleaching peaks on the TA spectra of composite crystals at ~520 nm can be attributed to the reduced crystal size of $CsPbBr_3$ on $CsPb_2Br_5$ with a lower proportion of CsBr in the precursor materials, which is consistent with the steady-state absorption and PL results given in Fig. S5 [variation (i)]. For perovskite materials, the time scale of the radiative decay process is in the range of a few hundred picoseconds to several nanoseconds. No obvious decay happens at the bleaching peaks of $CsPbBr_3$ crystals during the time region of 0–160 ps, illustrating that there is not any energy transition or carrier migration in the $CsPbBr_3$ reference crystals. However, for the $CsPb_2Br_5/CsPbBr_3$ composite crystals, the bleaching peaks have partially decayed to less than 100 ps, which means that the population of electrons at the excited states of composite crystals is reduced [variation (ii)]. Also, the spectral narrowing of bleaching peaks dominantly occurs, proving the carrier migration and reduction of occupied excited states [variation (iii)]. These results indicate that there must have an electron transfer process initiated from the excited states of $CsPbBr_3$ in the composite crystals. However, the excited-state absorption peaks of the composite crystals are reduced compared to that of the $CsPbBr_3$ reference crystals, signifying that the electron transitions from low excited states to high-excited states suppressed in $CsPbBr_3$ of the composited crystals [variation (iv)]. It is worth mentioning that apparent absorption signals are emerging at ~536 nm in the TA spectra of the composite crystals [Figs. S7(b) and S7(c)]. The peak is located at the low energy side of bleaching peaks during the time region of 10 ps, which can be attributed to the interfacial states of $CsPbBr_3$ in the composite crystals. For a semiconductor material, the change of strain and diffusion-induced non-stoichiometry at the interface would result in the spatial variation in the local interface band structure,[26,27] capable of changing the bandgap as large as 0.1 eV.[28] Thus, a new TA signal with a lower energy of ~0.05 eV is observed beside the bleaching peak of the bandgap. Simultaneously, Fig. 2(e) shows the TA spectra of the composite crystals within the initial 5 ps, from which we can see a dramatic evolution at the interfacial states. Figure 2(f) gives the corresponding TA signal

kinetics of band edge (~522 nm) and interfacial states (~536 nm). Upon photo-excitation, electron–hole pairs undergo a dissociation process. The Coulombically bound carriers are then dissociated into mobile charges with the help of photon energy, taking ~2 ps rise in the TA kinetics.[2] At the initial pumping stage of 0–0.55 ps, with the extraction of electrons from the ground state to the excited states in $CsPbBr_3$ of the composite crystals, the excited carriers migrate to the interface between $CsPbBr_3$ and $CsPb_2Br_5$, resulting in the gradually increased excited-state absorption signals of interfacial states. However, with the continuous accumulation of electrons to the excited states, the electrons at the interfacial states are sequentially pumped to the excited states of $CsPb_2Br_5$. That is why the absorption signals of interfacial states decrease dramatically and then turn into weak bleaching signals within 0.55–2 ps as displayed in Fig. 2(f). The inset of Fig. 2(e) presents the energy band diagram, illustrating the electron transition process at the interfacial states within 0–2 ps. Subsequently, the route to the high-excited states (excited-state absorption in $CsPbBr_3$ at 500–510 nm in Fig. S7) has also been impeded within 5–100 ps, evidencing that the electrons can only go to the excited states of $CsPb_2Br_5$ in the composite crystals. The absorption bleaching partially decays during the initial 100 ps, suggesting that only approximately half of the charge carriers have been transferred to the excited states of $CsPb_2Br_5$ crystals during this time, while the remaining part will decay or be transferred after 160 ps. Bleaching states in the TA spectra can be matched to the absorption peaks of the steady absorption spectrum.[29,30] Therefore, it is interesting to observe that the bleach signal at 536 nm for the composite crystals can be matched to the steady-state absorption peak at ~540 nm, as depicted in Fig. S5(e). This phenomenon suggests that the two states are correlated. Also, the small absorption peak located at ~360 nm can be attributed to the interfacial states of $CsPb_2Br_5$ crystals. All these findings prove another time that energy transitions and carrier migration occurred between $CsPb_2Br_5$ and $CsPbBr_3$ in the composite crystals.

On the other hand, the optical TA spectroscopy can directly measure the carrier concentration, which is strongly dependent on the band filling and population distribution of carriers.[31] Hence, it is impossible to conclude the population kinetics alone if the decay is due to the decreased conductivity or to the relaxation of carrier mobility with time. Since the THz radiation closely matches the typical carrier scattering rates of $10^{12}$–$10^{14}$ $s^{-1}$, it can directly interact with free carriers, elucidating the evolution of free carriers with more accurate data modeling.[32,33] The THz response is a product of carrier concentration and mobility. The time-resolved THz spectroscopy (TRTS) measurements correlating with the TA spectra can avoid overlapping different spectral components of the excited-state populations.[34] For further probing the kinetics of free carriers transferred in the composite crystals, TRTS is carried out to measure the local change in the photoconductivity, proportional to the carrier density as a function of time delay after excitation. Different from the TA measurement, the 266 nm pump source with the irradiation condition $\langle N \rangle = 1$ (~58 $\mu J\ cm^{-2}$ at 266 nm) is employed in TRTS to investigate the photo-excited charge carriers' kinetics of both $CsPb_2Br_5$ and $CsPbBr_3$ in the composite crystals, which coexist in the THz frequency range.[35] Figure 3 shows the TRTS spectra of the crystals, and it is witnessed that the THz absorption signals of $CsPb_2Br_5$ are mainly located at 40–80 $cm^{-1}$. Meanwhile, the signals from $CsPbBr_3$ are in the range of 130–350 $cm^{-1}$. Studying these phonon modes in the THz range is important because these phonons contribute to photoconductivity in the same frequency range as the free carriers.[33] Then, the plasmon-like response can be described by a Lorentz damped harmonic oscillator function

$$\sigma(\omega) = -i\varepsilon_0\omega(\varepsilon_\infty - 1) + \sum_{m=3\ or\ 5}, \frac{i\omega_{p,m}\omega}{\omega^2 - \omega_{0,m}^2 + i\frac{\omega}{\tau_m}}, \tag{2}$$

where $\omega_{p,m}$, $\omega_{0,m}$, and $\tau_m$ are the plasma frequencies, phonon resonance frequencies, and phonon scattering time of each oscillator, respectively.[33] Here, we use 3–5 Lorentzian oscillators, which fit the curves well in Fig. 3(d). The fitting parameters are also listed in Table I. The phonon resonance frequencies and the scattering times of $CsPb_2Br_5$ are all located in the low THz range. However, the phonon resonance in $CsPbBr_3$ occupies the higher THz frequencies. The oscillator modes in the composite crystals spread over both low and high THz frequencies, indicating that both $CsPb_2Br_5$ and $CsPbBr_3$ determine the oscillator activities in the composite crystals. According to the recent DFT calculations of infrared-active modes, the primary peaks located at ~60 $cm^{-1}$ (~2 THz) can be attributed to the vibration and interaction of the inorganic framework of lead and halogen, such as the distortions of the octahedra due to changes in the Br–Pb–Br bond angles and the changes in the Pb–Br bond lengths.[36,37] To be specific, the transverse vibration and the longitudinal optical vibrations of the Pb–Br–Pb bonds are located at 26 $cm^{-1}$ (0.8 THz) and 46.2 $cm^{-1}$ (1.4 THz), respectively. Moreover, the optical Br vibration is responsible for the peak at 66 $cm^{-1}$ (2.0 THz).[38] For the moment, the peaks with a frequency higher than 150 $cm^{-1}$ (~4 THz) can be attributed to the vibration and torsional modes of cations in perovskites.[33,39,40] In $CsPb_2Br_5$, there is a layered 2D structure of Pb–Br bonds and Cs cations. Then, the THz absorption signals are mainly located in a frequency less than 80 $cm^{-1}$. Nevertheless, $CsPbBr_3$ has a 3D structure with the vibration of the $PbBr_6$ octahedron contributing to the THz absorption at ~112 $cm^{-1}$ (~3.4 THz) and the vibration of $Cs^+$ strongly affecting the properties of the crystal.[35] Therefore, the THz absorption signal is in a wide range of 130–350 $cm^{-1}$. The THz absorption signals of the composite crystals integrate with the individual absorption signals of $CsPb_2Br_5$ and $CsPbBr_3$ crystals, as shown in Fig. 3(d). Intrinsic peak photoconductivity values can be obtained using the following equation:[31,35]

$$\Delta\sigma(t_p) = \frac{\varepsilon_0 c}{d}(n_a + n_b)\frac{-\Delta E(t_p)}{E_0(t_p)}, \tag{3}$$

where $\varepsilon_0$ is the permittivity of free space, $c$ is the speed of light, $d$ is the thickness of the photo-excited sample, and $n_a$ and $n_b$ are the refractive indices of the media on either side of the sample. The value of $\Delta E/E$ is proportional to the photoconductivity, which is linearly dependent on the product of density and mobility of the photogenerated free carriers.

The normalized signal kinetics of transient photoconductivity of the crystals are calculated and plotted in Fig. 4. For the $CsPb_2Br_5$ crystals, the indirect bandgap and the excellent crystal quality provide less pathway for the photo-induced carriers to recombine with short time constants. Hence, the carrier relaxation process in $CsPb_2Br_5$ would last for a long time. Nonetheless, the photoconductivity lifetime of $CsPb_2Br_5$ is dramatically

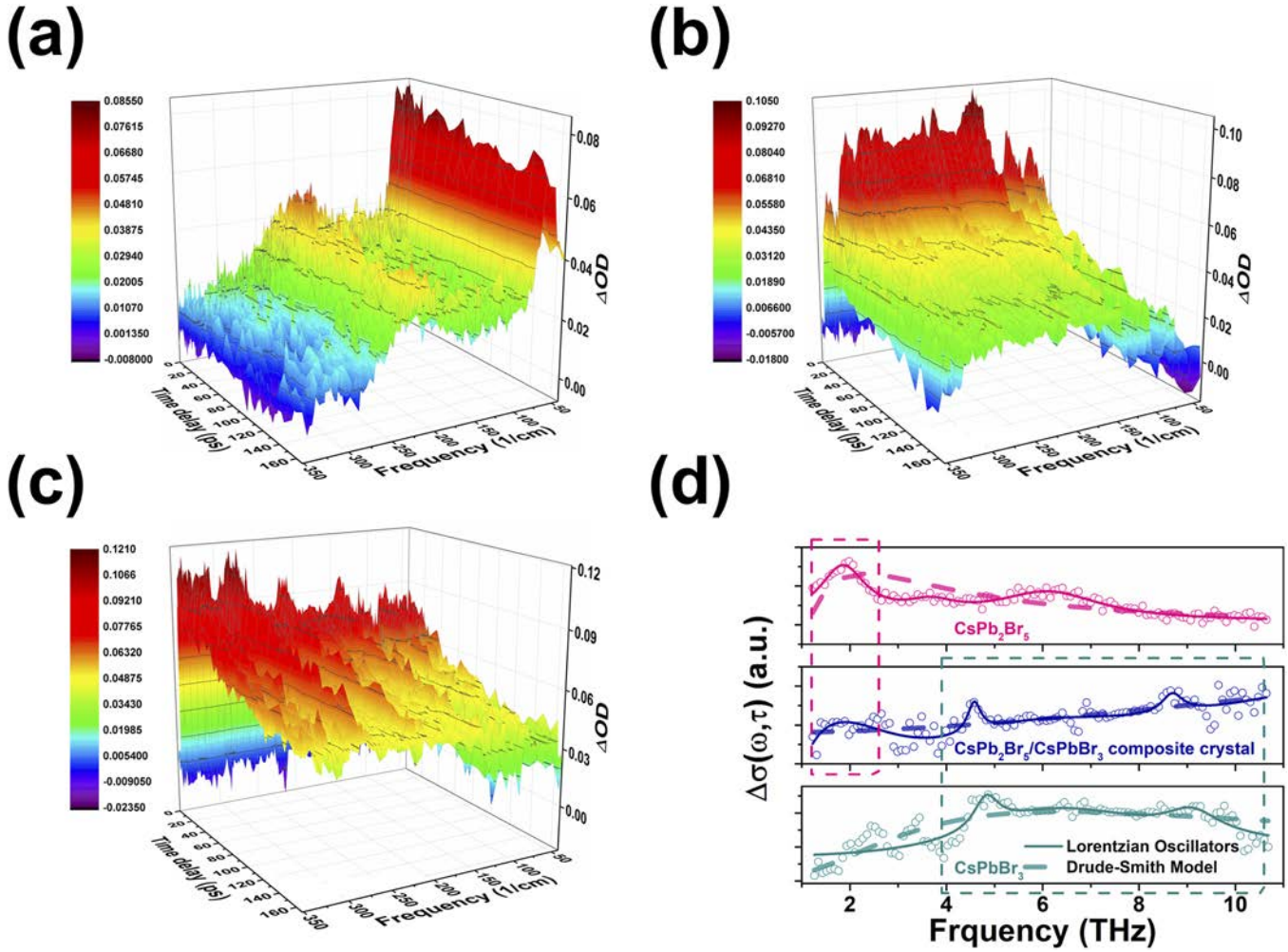


**FIG. 3.** Time-resolved THz spectroscopy of $CsPb_2Br_5$ (a), $CsPbBr_3$ (b), and $CsPb_2Br_5/CsPbBr_3$ composite crystals (c) synthesized with the precursor ratio ($CsBr:PbBr_2$) of 0.8:1. (d) Frequency dependent THz photo-conductance spectra of $CsPb_2Br_5$, $CsPbBr_3$, and $CsPb_2Br_5/CsPbBr_3$ composite crystals with the time delay of 10 ps. The solid lines are fitting results with 3–5 Lorentz oscillators, dash lines are the fits to the Drude–Smith model.

**TABLE I.** Lorentzian parameters to describe THz conductivity.

| | Peak number (m) | $\omega_{0,m}$ (THz) | $\tau_m$ (s) | $\omega_{p,m}$ (THz) |
|---|---|---|---|---|
| $CsPb_2Br_5$ | 1 | 1.793 89 | $7.596\,59 \times 10^{-13}$ | 9.515 62 |
| | 2 | 3.772 11 | $7.445\,63 \times 10^{-13}$ | 2.178 74 |
| | 3 | 6.104 95 | $3.884\,61 \times 10^{-13}$ | 9.258 07 |
| $CsPbBr_3$ | 1 | 4.830 4 | $1.519\,71 \times 10^{-12}$ | 4.357 55 |
| | 2 | 6.483 87 | $1.985\,08 \times 10^{-13}$ | 46.811 4 |
| | 3 | 9.110 26 | $7.263\,38 \times 10^{-13}$ | 6.436 34 |
| $CsPb_2Br_5/CsPbBr_3$ composite crystals | 1 | 1.644 59 | $2.511\,77 \times 10^{-13}$ | 112.922 |
| | 2 | 4.576 66 | $2.883\,37 \times 10^{-12}$ | 1.354 34 |
| | 3 | 5.88 | $1.630\,98 \times 10^{-13}$ | 53.043 1 |
| | 4 | 6.242 45 | $2.703 \times 10^{-15}$ | 189.396 |
| | 5 | 8.69 | $1.832\,01 \times 10^{-12}$ | 1.361 3 |

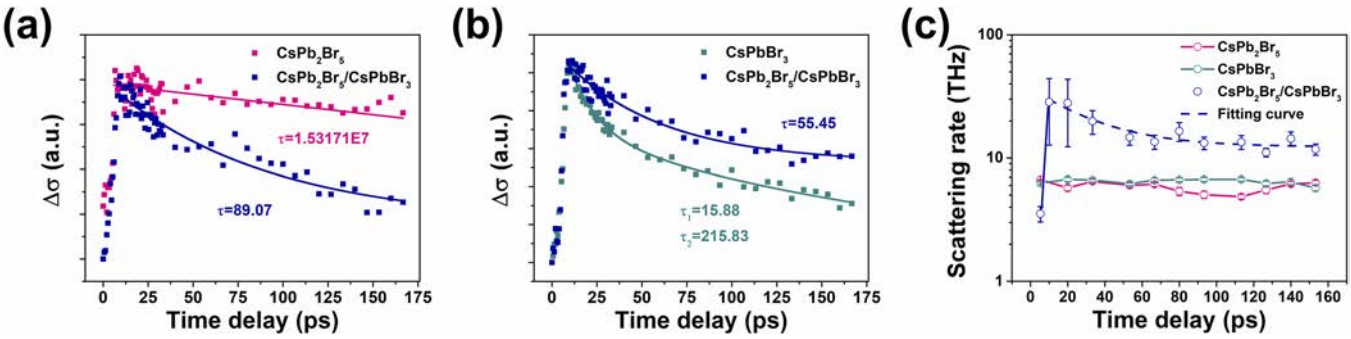


**FIG. 4.** Normalized signal kinetics of transient photoconductivity in $CsPb_2Br_5$, $CsPbBr_3$, and $CsPb_2Br_5/CsPbBr_3$ composite crystals [synthesized with the precursor ratio ($CsBr:PbBr_2$) of 0.8:1]. (c) Time-dependence of the scattering time extracted from the Drude–Smith fit.

decreased in the composite crystals, which illustrates that the presence of $CsPbBr_3$ has introduced an effective way in $CsPb_2Br_5$ for hot carriers to transfer. These hot carriers in $CsPb_2Br_5$ are most likely to relax to the excited states of $CsPbBr_3$, then participate in the luminescence process. For the $CsPbBr_3$ crystals, there are two decay lifetimes of their photoconductivity. The fast one of 15.88 ps can be attributed to the Auger recombination process, which is a fast, multi-electron, non-radiative recombination pathway that enables one hot carrier to decay by transferring its energy to other excited carriers with a time constant of 10–100 ps under high irradiation condition ($\langle N \rangle = 1$).[41,42] Meanwhile, the slow decay time of 215.83 ps should originate from other defect-related non-radiative processes in the crystals. The radiative process of $CsPbBr_3$ crystals may last for several nanoseconds. Also, the non-radiative process is usually faster than the radiative ones.[39,43,44] For example, the carriers in $MAPbI_3$ relax to localized states of I dangling bond typically have the time scale of 230 ps, which corresponds to the time scale of the non-radiative process in the $CsPbBr_3$ crystals.[39] Anyway, after being combined with $CsPb_2Br_5$, the $CsPbBr_3$ in the composite crystals have only one migration process with a lifetime of 55.45 ps, which can be ascribed to the decreased Auger recombination, indicating that the non-radiative recombination is significantly suppressed. The rapid Auger recombination is the main reason for the efficiency roll-off of the perovskite light-emitting diodes (PeLEDs).[45] When combined with $CsPb_2Br_5$, the electron–hole wavefunction overlap in $CsPbBr_3$ is reduced; then, the Auger recombination rate would decrease from 63 to 18 MHz. This suppressed Auger recombination as well reduces the Joule heating in materials, thus directly explaining the enhanced PL quantum yield and stability of the $CsPb_2Br_5/CsPbBr_3$ composite crystals. Besides, it is well known that the presence of Br vacancies ($V_{Br}$) on the surface of $CsPbBr_3$ generates defects within the bandgap, which could act as recombination centers and quench the emission by accelerating the non-radiative charge recombination.[5,11,19] Notably, the photoconductance of $CsPbBr_3$ in the composite crystals has only one Auger recombination pathway, which means that the $CsPb_2Br_5$ can effectively passivate the $V_{Br}$ defects, shutting down the deep-level defects related non-radiative process. Both the suppressed Auger recombination rate and the defect-related non-radiative process can contribute to the reported high PL quantum yield of the $CsPb_2Br_5/CsPbBr_3$ composite materials.

Furthermore, the conductivities of crystals are governed by the influence of disorder on the free-carrier dynamics, which is usually well-described by the Drude–Smith model as described in the following:

$$\Delta\sigma(\omega,\tau) = \frac{\varepsilon_0 \omega_p^2}{\Gamma - i\omega}\left[1 + \frac{c_1}{1 - i\omega/\Gamma}\right], \tag{4}$$

where the first term is the Drude conductivity, while the second Smith term modifies the Drude model by accounting for the backscattering of carriers ($c_1$ is negative). $\Gamma$ denotes the scattering rate of the free carriers, which is related to the electron momentum scattering with phonons. The extracted free carrier scattering rates from the Drude–Smith model are then plotted in Fig. 4(c). The scattering times of both $CsPb_2Br_5$ and $CsPbBr_3$ are stable throughout the entire window, which means that the mobility is essentially constant over this range of time delays. However, it is observed that there is an initial increase in the scattering rate within 15 ps for the composite crystals, which gradually flattens off and reaches a steady value by ~100 ps. The initial growth of the mobility can be attributed to the initial thermalization of hot carriers discussed above. The scattering rate in the composite crystals is higher than other crystals by orders of magnitude due to the higher population of the optical phonons. Besides, the Drude–Smith model reflects the nature of the scattering processes and the presence of excess phonons in materials. The interfacial states, or shallow defects, increase the scattering processes, thereby stimulating the time between collisions and resulting in higher scattering rates.[46] In the composite crystals, the charge transport between two perovskites is no longer free propagation. It is governed by phonon scattering-assisted hopping of electrons between these states, which is known as the hopping mechanism widely observed in low-dimensional and disordered materials.[47–49] The decay time of the scattering rate is ~65 ps, which refers to the carriers hopping time constant that is also in accord with the decay time of photoconductance. These results can provide direct evidence that the hot carriers can be transferred between $CsPb_2Br_5$ and $CsPbBr_3$ with a time scale of 60–90 ps.

The emission mechanism of the composite crystals can be illustrated by an electron transition model in the energy level diagrams of $CsPb_2Br_5/CsPbBr_3$ concluded from the ultra-fast spectroscopy (Fig. 5). Unlike the energy level system of a single $CsPbBr_3$, the

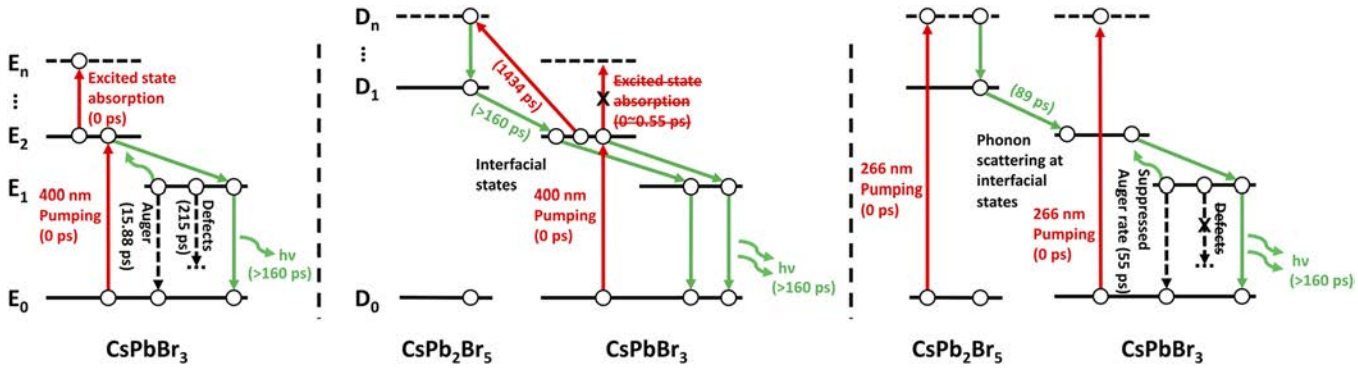


**FIG. 5.** Energy level diagram of electron transition in $CsPb_2Br_5/CsPbBr_3$ composite crystals.

excited-state electrons in the composite crystals can be pumped to the excited states in $CsPb_2Br_5$ instead in the early stage of the pumping process. The narrowed and decayed bleaching spectrum can also prove this inference. The lifetime of 1434 ps is due to the continuous photo-induced carrier migration by the probe beam.[25,42] The electrons populated on the $D_1 \sim D_n$ level can relax to the $E_n$ level owing to the relatively closed energy states, confirmed by the dramatically decreased photoconductivity lifetime of $CsPb_2Br_5$. This lifetime of the radiative recombination process is determined to be >160 ps because there is no incident observed for this process during the time region of 1–160 ps. In the composite crystals, the dominant electron transfer process is the intersystem crossing (ISC), and the $CsPb_2Br_5$ and $CsPbBr_3$ interact more with each other. More carriers will participate in the luminescent process, yielding the enhanced fluorescence and quantum yield in the $CsPb_2Br_5/CsPbBr_3$ composite crystals. Consequently, the green emission of the composite crystals can be substantially enhanced.[6,8,9]

## CONCLUSION

In summary, single-phase high-quality $CsPb_2Br_5$ crystals have been successfully prepared by a microwave-assisted synthesis method. The luminescence-inactive characteristics of $CsPb_2Br_5$ are evidently confirmed. Importantly, the prepared $CsPb_2Br_5$ crystals present high crystallinity and enhanced thermal stability. Even after immersing the crystals in ethanol and acetone, they can still maintain their crystalline structures well. By characterizing and investigating the fluorescent activities of the samples prepared with different ratios of precursor materials, it is found that the green emission comes from the $CsPbBr_3$ adhered, nucleated, and grown on the $CsPb_2Br_5$ crystals. Ultrafast transient absorption measurements of the samples have then been taken, and the electron migration at the interfacial states is observed by the TA spectra. The phonon scattering-assisted hopping at the interfacial states is verified by TRTS, where the presence of $CsPbBr_3$ is determined to introduce an effective way in $CsPb_2Br_5$ for the transfer of hot carriers. The intersystem crossing dominates the electron transfer process in the composite crystals; therefore, the $CsPb_2Br_5$ and $CsPbBr_3$ in the composite crystals interact extensively with each other. Meanwhile, the Auger recombination rate and the defect-related non-radiative process are found to be suppressed in the composite crystals, thereby enhancing the fluorescence of the composite crystals. These results have deconvoluted the controversial and unclear luminescent mechanisms of the $CsPb_2Br_5$ materials and shown a pathway to design and enhance the fluorescence of materials.

## EXPERIMENTAL SECTION

### Microwave-assisted synthesis of pure $CsPb_2Br_5$ crystals

In order to obtain the pure $CsPb_2Br_5$ crystals without PbBr microwires or $CsPbBr_3$ crystals, a microwave-assisted synthesis method was adopted. $PbBr_2$ (99.0%) and CsBr (99.9%) were purchased from Sigma-Aldrich, in which they were used as received without any further purification or treatment. First, a saturated aqueous solution of $PbBr_2$ was prepared in a 25 ml beaker as the mother liquor (0.001 mol $PbBr_2$, 15 ml deionized water). Then, the mother liquor was taken into a microwave oven and pre-heated to about 90 °C. Subsequently, 10 ml of CsBr solution (0.0005 mol) was added to the mother liquor with an intense stirring. The mixed solution was heated in the microwave oven again for 10 s. The solution was next naturally cooled for 3 min while the $CsPb_2Br_5$ crystals began to separate out from the solution. Finally, the supernatant was transferred by a pipette and dropped onto the substrates (e.g., glass, silicon, or sapphire). The $CsPb_2Br_5$ crystals were obtained after drying the samples at 60 °C.

### Microwave-assisted synthesis of $CsPb_2Br_5/CsPbBr_3$ composite crystals

A similar synthesis procedure was developed for the growth of $CsPb_2Br_5/CsPbBr_3$ composite crystals. The crucial factor to obtain the $CsPb_2Br_5/CsPbBr_3$ composite crystals, instead of the pure $CsPb_2Br_5$ crystals, is the precise control of molar ratio of the precursor materials. In this case, the saturated aqueous solution of $PbBr_2$ was first prepared and pre-heated (0.001 mol $PbBr_2$, 15 ml deionized water). Then, different amounts of CsBr (i.e., 0.0006, 0.0007, and 0.0008 mol) were dissolved into 10 ml of water and separately added into the pre-heated $PbBr_2$ solution with an intense stirring.

The molar ratios of CsBr and $PbBr_2$ in the mixed precursor solutions were 0.6:1, 0.7:1, and 0.8:1, respectively. After heating in microwave oven for 10 s and natural cooling for 3 min, the supernatant was also transferred onto substrates and dried at 60 °C.

### Synthesis of $CsPbBr_3$ crystals for reference

The $CsPbBr_3$ crystals used as a reference for the optical characterization and analysis were grown by a one-step chemical vapor deposition (CVD) method in vacuum ambiance. $CsBr_2$ (99.9%, Sigma-Aldrich) and PbBr (99.9%, Sigma-Aldrich) powder were thoroughly mixed with a molar ratio of 1:1, then put into an alumina boat to act as the reactant source. Well-cleaned substrates (glass or quartz, 10 × 10 $mm^2$) were placed on the downstream side of the furnace. The distance between the source boat and the substrate was 12 cm. Before heating, the quartz tube was pumped down to 150 Pa. High-purity argon (99.999%) was used as a carrier gas to transport the reactant vapor to downstream. For the growth of high-quality $CsPbBr_3$ crystals, the flow rate was optimized at 150 SCCM. Then, the furnace was heated to 600 °C with a temperature gradient of 20 °C/min and held for a duration of 15 min. After natural cooling to room temperature, the $CsPbBr_3$ crystals were identified on the substrate.

### Characterization

The morphology of the sample was testified by an Olympus FV1000 confocal laser scanning microscope. The XRD characterization was performed on a Bruker D8 system using Cu-ka radiation. The absorption spectra were collected by a Shimadzu UV-3101PC spectrometer. The PL measurement was carried out with a Hitachi F-7000 fluorescence spectrophotometer. The light pulses (800 nm, 35 fs, 1 kHz repetition rate) of the ultrafast femtosecond transient absorption spectra were generated by a regenerative amplifier (Spitfire Ace) seeded by a femtosecond oscillator (Mai Tai, spectra physics). The fundamental output of the laser was split into two beams. One was used to generate the pump pulses (400 nm) by an optical parametric amplifier (Tropas, spectra physics), while the other one (1 $\mu$J/pulse) was focused on the water to generate the probe light. The entire experiment was done at room temperature.

### TRTS measurements

A commercial laser with 100 fs pulse width, 1 kHz repetition frequency, and 800 nm output wavelength is served as the light source of the THz transient spectroscopy system. The laser was separated into three beams, one of which was frequency-doubled to 400 nm and then mixed with another 800 nm pulses to generate broadband femtosecond infrared light (30–350 $cm^{-1}$) in the air. The 266 nm pumping source was generated from the third 800 nm beam by a triple frequency module of Eskma company. Broadband single shot probe light was recorded by an Andor EMCCD (Oxford Instruments) with the assistance of nonlinear up-conversion. As shown in Fig. S8, the probe light ($E_{signal}$) and femtosecond laser beam ($E_{reference}$) are combined and focused in a xenon container with one bar pressure to form the filamentous plasma, producing a third-order nonlinear process called four waves mixing ($\omega_1 + \omega_1 - \omega_0 = \omega_2$). Then, a nonlinear spectral up-conversion is achieved, allowing direct detection across the entire source spectral range in the frequency domain without Fourier transformation.

For the linear Fourier transform, the variation of the THz electric field in the time domain, denoted as

$$\Delta E(t_p) = E(t_p) - E_0(t_p), \tag{5}$$

can be represented in the frequency domain as

$$\hat{\mathcal{F}}(\Delta E(t_p)) = \hat{\mathcal{F}}(E(t_p)) - \hat{\mathcal{F}}(E_0(t_p)) = A(t) - A_0(t), \tag{6}$$

where $A(t)$ is the amplitude at time $t$ in the frequency domain. Then, we get the following relationship:

$$\Delta\sigma(\omega, t) \propto \frac{\varepsilon_0 c}{d}(n_a + n_b)\Delta OD\ (optical\ density). \tag{7}$$

## SUPPLEMENTARY MATERIAL

See the supplementary material for a schematic diagram of the microwave-assisted synthetic process and the nonlinear up-conversion testing method; structural and steady-state optical properties of the crystals; microscopy images and EDX spectra of the $CsPb_2Cr_5$ and composite crystals; XRD patterns, SEM images, and time-resolved transient absorption spectra of the reference $CsPbCr_3$ crystals and the composite crystals synthesized with the different precursor ratios.

## ACKNOWLEDGMENTS

This work was supported by the National Natural Science Foundation of China under Grant Nos. 11874351, 11874352, and 51672229; the Hong Kong Scholars Program (Grant No. XJ2019027); a fellowship award from the Research Grants Council of the Hong Kong Special Administrative Region, China (CityU RFS2021-1S04); and the Foshan Innovative and Entrepreneurial Research Team Program (Grant No. 2018IT100031).

## AUTHOR DECLARATIONS

### Conflict of Interest

The authors have no conflicts to disclose.

### Author Contributions

Y.W. and F.W. contributed equally to this work.

## DATA AVAILABILITY

The data that support the findings of this study are available from the corresponding authors upon reasonable request.

## REFERENCES

[1] S. Yakunin, L. Protesescu, F. Krieg, M. I. Bodnarchuk, G. Nedelcu, M. Humer, G. De Luca, M. Fiebig, W. Heiss, and M. V. Kovalenko, Nat. Commun. **6**, 8056 (2015).
[2] C. S. Ponseca, Jr., T. J. Savenije, M. Abdellah, K. Zheng, A. Yartsev, T. Pascher, T. Harlang, P. Chabera, T. Pullerits, A. Stepanov, J.-P. Wolf, and V. Sundström, J. Am. Chem. Soc. **136**(14), 5189–5192 (2014).
[3] L. Protesescu, S. Yakunin, M. I. Bodnarchuk, F. Krieg, R. Caputo, C. H. Hendon, R. X. Yang, A. Walsh, and M. V. Kovalenko, Nano Lett. **15**(6), 3692–3696 (2015).

[4]Y. Jiang, B. Li, T. Zhang, Y. Shi, and Q. H. Xu, ChemNanoMat **6**(3), 327–335 (2020).
[5]Y. Tan, R. Li, H. Xu, Y. Qin, T. Song, and B. Sun, Adv. Funct. Mater. **29**(23), 1900730 (2019).
[6]S. Lou, Z. Zhou, T. Xuan, H. Li, J. Jiao, H. Zhang, R. Gautier, and J. Wang, ACS Appl. Mater. Interfaces **11**(27), 24241–24246 (2019).
[7]B.-S. Zhu, H.-Z. Li, J. Ge, H.-D. Li, Y.-C. Yin, K.-H. Wang, C. Chen, J.-S. Yao, Q. Zhang, and H.-B. Yao, Nanoscale **10**(41), 19262–19271 (2018).
[8]G. Jiang, C. Guhrenz, A. Kirch, L. Sonntag, C. Bauer, X. Fan, J. Wang, S. Reineke, N. Gaponik, and A. Eychmüller, ACS Nano **13**(9), 10386–10396 (2019).
[9]K. Du, L. He, S. Song, J. Feng, Y. Li, M. Zhang, H. Li, C. Li, and H. Zhang, Adv. Funct. Mater. **31**(36), 2103275 (2021).
[10]X. Tang, Z. Hu, W. Yuan, W. Hu, H. Shao, D. Han, J. Zheng, J. Hao, Z. Zang, J. Du, Y. Leng, L. Fang, and M. Zhou, Adv. Opt. Mater. **5**(3), 1600788 (2017).
[11]X. Zhang, Z. Jin, J. Zhang, D. Bai, H. Bian, K. Wang, J. Sun, Q. Wang, and S. F. Liu, ACS Appl. Mater. Interfaces **10**(8), 7145–7154 (2018).
[12]Z.-P. Huang, B. Ma, H. Wang, N. Li, R.-T. Liu, Z.-Q. Zhang, X.-D. Zhang, J.-H. Zhao, P.-Z. Zheng, Q. Wang, and H.-L. Zhang, J. Phys. Chem. Lett. **11**(15), 6007–6015 (2020).
[13]Z.-L. Yu, Y.-Q. Zhao, Q. Wan, B. Liu, J.-L. Yang, and M.-Q. Cai, J. Phys. Chem. C **124**(42), 23052–23058 (2020).
[14]C. Qin, T. Matsushima, A. S. D. Sandanayaka, Y. Tsuchiya, and C. Adachi, J. Phys. Chem. Lett. **8**(21), 5415–5421 (2017).
[15]K.-H. Wang, L. Wu, L. Li, H.-B. Yao, H.-S. Qian, and S.-H. Yu, Angew. Chem., Int. Ed. **55**, 8328–8332 (2016).
[16]Y.-Q. Zhou, J. Xu, J.-B. Liu, and B.-X. Liu, J. Phys. Chem. Lett. **10**(20), 6118–6123 (2019).
[17]C. Wang, Y. Wang, X. Su, V. G. Hadjiev, S. Dai, Z. Qin, H. A. Calderon Benavides, Y. Ni, Q. Li, J. Jian, M. K. Alam, H. Wang, F. C. Robles Hernandez, Y. Yao, S. Chen, Q. Yu, G. Feng, Z. Wang, and J. Bao, Adv. Mater. **31**(33), 1902492 (2019).
[18]T. Zhang, Z. Chen, Y. Shi, and Q.-H. Xu, Nanoscale **11**(7), 3186–3192 (2019).
[19]X. Zhang, B. Xu, J. Zhang, Y. Gao, Y. Zheng, K. Wang, and X. W. Sun, Adv. Funct. Mater. **26**(25), 4595–4600 (2016).
[20]I. Bilecka and M. Niederberger, Nanoscale **2**(8), 1358–1374 (2010).
[21]P. Lidström, J. Tierney, B. Wathey, and J. Westman, Tetrahedron **57**, 9225–9283 (2001).
[22]R. Berera, R. van Grondelle, and J. T. Kennis, Photosynth. Res. **101**(2–3), 105–118 (2009).
[23]V. I. Klimov, J. Phys. Chem. B **104**(26), 6112–6123 (2000).
[24]T. Debnath, S. Maiti, P. Maity, and H. N. Ghosh, J. Phys. Chem. Lett. **6**(17), 3458–3465 (2015).
[25]H. Chung, S. I. Jung, H. J. Kim, W. Cha, E. Sim, D. Kim, W.-K. Koh, and J. Kim, Angew. Chem., Int. Ed. **56**(15), 4160–4164 (2017).
[26]L. Brillson, Surf. Sci. Rep. **2**(2), 123–326 (1982).
[27]J. S. Blakemore, J. Appl. Phys. **53**(10), R123–R181 (1982).
[28]L. D. Bell and W. J. Kaiser, Phys. Rev. Lett. **61**(20), 2368–2371 (1988).
[29]S. A. Miller, J. M. Womick, J. F. Parker, R. W. Murray, and A. M. Moran, J. Phys. Chem. C **113**, 9440–9444 (2009).
[30]S. H. Yau, N. Abeyasinghe, M. Orr, L. Upton, O. Varnavski, J. H. Werner, H.-C. Yeh, J. Sharma, A. P. Shreve, J. S. Martinez, and T. Goodson III, Nanoscale **4**(14), 4247–4254 (2012).
[31]S. Sarkar, V. K. Ravi, S. Banerjee, G. R. Yettapu, G. B. Markad, A. Nag, and P. Mandal, Nano Lett. **17**(9), 5402–5407 (2017).
[32]C. La-o-vorakiat, T. Salim, J. Kadro, M.-T. Khuc, R. Haselsberger, L. Cheng, H. Xia, G. G. Gurzadyan, H. Su, Y. M. Lam, R. A. Marcus, M.-E. Michel-Beyerle, and E. E. M. Chia, Nat. Commun. **6**, 7903 (2015).
[33]C. La-o-vorakiat, H. Xia, J. Kadro, T. Salim, D. Zhao, T. Ahmed, Y. M. Lam, J.-X. Zhu, R. A. Marcus, M.-E. Michel-Beyerle, and E. E. M. Chia, J. Phys. Chem. Lett. **7**(1), 1–6 (2016).
[34]J. Peng, Y. Chen, K. Zheng, T. Pullerits, and Z. Liang, Chem. Soc. Rev. **46**(19), 5714–5729 (2017).
[35]G. R. Yettapu, D. Talukdar, S. Sarkar, A. Swarnkar, A. Nag, P. Ghosh, and P. Mandal, Nano Lett. **16**(8), 4838–4848 (2016).
[36]A. M. A. Leguy, A. R. Goñi, J. M. Frost, J. Skelton, F. Brivio, X. Rodríguez-Martínez, O. J. Weber, A. Pallipurath, M. I. Alonso, M. Campoy-Quiles, M. T. Weller, J. Nelson, A. Walsh, and P. R. F. Barnes, Phys. Chem. Chem. Phys. **18**(39), 27051–27066 (2016).
[37]D. Zhao, J. M. Skelton, H. Hu, C. La-o-vorakiat, J.-X. Zhu, R. A. Marcus, M.-E. Michel-Beyerle, Y. M. Lam, A. Walsh, and E. E. M. Chia, Appl. Phys. Lett. **111**(20), 201903 (2017).
[38]I. Maeng, S. Lee, H. Tanaka, J.-H. Yun, S. Wang, M. Nakamura, Y.-K. Kwon, and M.-C. Jung, NPG Asia Mater. **12**(1), 53 (2020).
[39]J. Wang, W. Li, and W. J. Yin, Adv. Mater. **32**(6), 1906115 (2020).
[40]C. Quarti, G. Grancini, E. Mosconi, P. Bruno, J. M. Ball, M. M. Lee, H. J. Snaith, A. Petrozza, and F. De Angelis, J. Phys. Chem. Lett. **5**(2), 279–284 (2014).
[41]G. E. Eperon, E. Jedlicka, and D. S. Ginger, J. Phys. Chem. Lett. **9**(1), 104–109 (2018).
[42]N. S. Makarov, S. Guo, O. Isaienko, W. Liu, I. Robel, and V. I. Klimov, Nano Lett. **16**(4), 2349–2362 (2016).
[43]A. Liu and Y. Rosenwaks, J. Appl. Phys. **86**(1), 430–437 (1999).
[44]R. Stachowitz, M. Schubert, and W. Fuhs, Phys. Rev. B **52**(15), 10906–10914 (1995).
[45]Y. Jiang, M. Cui, S. Li, C. Sun, Y. Huang, J. Wei, L. Zhang, M. Lv, C. Qin, Y. Liu, and M. Yuan, Nat. Commun. **12**(1), 336 (2021).
[46]M. C. Beard, G. M. Turner, and C. A. Schmuttenmaer, J. Appl. Phys. **90**(12), 5915–5923 (2001).
[47]I. V. Gornyi, A. D. Mirlin, and D. G. Polyakov, Phys. Rev. Lett. **95**(20), 206603 (2005).
[48]C. Schmidt, J. Bühler, A.-C. Heinrich, J. Allerbeck, R. Podzimski, D. Berghoff, T. Meier, W. G. Schmidt, C. Reichl, W. Wegscheider, D. Brida, and A. Leitenstorfer, Nat. Commun. **9**(1), 2890 (2018).
[49]H. Qiu, T. Xu, Z. Wang, W. Ren, H. Nan, Z. Ni, Q. Chen, S. Yuan, F. Miao, F. Song, G. Long, Y. Shi, L. Sun, J. Wang, and X. Wang, Nat. Commun. **4**, 2642 (2013).